Constructing molecular junction in covalent organic frameworks for efficient uranium(VI) photoreduction

Zhi Gao [a,b], Yue Wang [a], Zhaodi Sun [a], Zhenzhen Xu [a,*], Jiajun Liao [a], Zhuyao Li [a], Yidong Luo [b], Long-Shuai Zhang [c,*], Jian-Ping Zou [c,*]

[a] School of Chemistry and Materials Science, East China University of Technology, Nanchang, Jiangxi 330013, China
[b] Foshan (Southern China) Institute for New Materials, Foshan, Guangdong 528000, China
[c] Key Laboratory of Jiangxi Province for Persistent Pollutants Control and Resources Recycle, Nanchang Hangkong University, Nanchang, Jiangxi 330063, China

ARTICLE INFO

ABSTRACT

Constructing heterojunction photocatalysts is widely regarded as an effective strategy to improve photocatalytic reduction efficiency of U(VI) to U(IV). However, the traditional heterojunctions fabricated by the multiphase hybridization generally present inhomogeneous junction distribution and low connectivity, which is not beneficial for the migration of photogenerated charges. Here, Cu-N cluster as oxidative site and Ti-O cluster as reductive site are covalently coupled to fabricate Cu_3-Ti_6-COF molecular junction. Importantly, the resulting Cu_3-Ti_6-COF not only possesses high connectivity but also exhibits well-defined crystalline structure and monophasic periodic distribution, thus effectively boosting the directed transport and separation of charge carriers. As a result, the excellent photocatalytic performance is achieved with the U(VI) removal efficiency of up to 94.8 % without any sacrificial reagents. As far as our knowledge, this is the first work about constructing COF molecular junction for photoreduction U(VI), which may simulate the exploration of novel COFs photocatalysts toward photoinduced radionuclide removal.

1. Introduction

Developing mild and green technology to effectively removal uranium from contaminated groundwater is of great significance for environmental remediation owing to the combined radioactivity and chemical toxicity of uranium wastewater [1,2]. On the other hand, the effective enrichment of uranium from wastewater is beneficial for the sustainable development of nuclear energy as uranium is a crucial resource in the nuclear fuel cycle [3–5]. Up to now, a variety of approaches including membrane separation [6], ionic exchange [7], adsorption [8], solvent extraction [9] and photocatalytic reduction [10–12] have been proposed to removal uranium. Among them, the photocatalytic reduction technology utilizing the large difference of solubility between U(VI) and U(IV) has been regarded as more promising strategy to removal uranium on account of its unique advantages such as simplicity, no secondary pollution, environmental friendliness and high efficiency [13–15].

As well known, heterojunction photocatalysts possess the excellent ability to separate photogenerated electron-hole and thus receive extensive attention in the photocatalytic fields. Various inorganic heterojunction composed of two different kinds of inorganic semiconductor have been widely designed to improve the efficiency of photoreduction U(VI) to U(IV) [16]. Regrettably, inorganic heterojunction often suffers from the low utilization of light absorption, less-exposed active sites owing to the relatively low surface area, and poor stability in complex radioactive wastewater [17]. Moreover, most of inorganic heterojunction are nanocomposites without well-defined structure, whose performances are affected by many factors including particle size, morphology, crystal face and so on, hindering the cross-validation between experimental and theoretical results. In addition, during the reaction process, the hole sacrificial agents such as methanol is often needed to trap the holes, thus promoting the generated electron to reduce U(VI). Regrettably, the addition of the hole sacrificial agents not only raise the cost of U(VI) photoreduction, but also results in the secondary chemical pollution [18]. As a result, exploring novel heterojunction photocatalysts to conquer above mentioned drawbacks is highly desired but remains huge challenges.

Covalent organic frameworks (COFs) as emerging crystalline porous

---

* Corresponding authors.
E-mail addresses: xu_zhenzhen@ecut.edu.cn (Z. Xu), L_S_Zhang1990@163.com (L.-S. Zhang), zjp_112@126.com (J.-P. Zou).

materials have the unique properties of high specific surface area, tunable structures and high stability [19–23], which make them ideal platforms to fabricate heterojunction photocatalysts toward photocatalytic reduction of U(VI) to U(IV) [24–26]. Unfortunately, these traditional COFs-based heterojunction photocatalysts are mostly constructed by the multiphase hybridization and thus show inhomogeneous junction distribution, which is not beneficial for the directed separation of photogenerated charges to the photocatalysts surface [27]. Moreover, the organic building units scarcely possess a high number (>4) of reactive sites to fabricate COFs with high connectivity [28], thus leading to the less electron-hole separation channel in the COFs-based heterojunction. By comparison, inspired by the design principles of heterojunctions, constructing heterojunction COFs photocatalysts with monophasic periodic distribution and rich charge separation and transfer channels should be an effective strategy to improve photocatalytic efficiency for U(VI) reduction without sacrificial agents.

Based on the above considerations, Ti_6 (6 connecting sites) and Cu_3 (3 connecting sites) clusters were elaborately synthesized as building units to construct Cu_3-Ti_6-COF molecular junction with high connectivity (Scheme 1). The small size of metal clusters as building blocks and the high connectivity of Cu_3-Ti_6-COF are beneficial for the charge carrier migration in the skeleton. Noticeably, different from the traditional heterojunction photocatalysts, the Cu_3-Ti_6-COF presents the well-defined structure and monophasic periodic distribution, in which the oxidative sites (Cu_3 cluster) for water oxidation and reductive sites (Ti_6 cluster) toward photoreduction U(VI) are spatially periodically separated at the molecular level. These unique merits of Cu_3-Ti_6-COF molecular junction greatly improve the directed transport and separation efficiency of photogenerated charges and consequently results in the outstanding photocatalytic activity. The U(VI) removal ratio of up to 94.8 % is achieved after visible light irradiation of 210 min without the addition of hole sacrificial agents in air atmosphere. Moreover, the good reusability and outstanding anti-interference ability for F^- and various organics is verified in Cu_3-Ti_6-COF.

2. Experimental section

2.1. Materials and characterizations

Powder X-ray diffraction (PXRD) patterns were taken on a Rigaku SmartLab SE X-ray diffractometer. Solid-state ^{13}C cross-polarization magic-angle spinning nuclear magnetic resonance (^{13}C CP/MAS NMR) spectra were collected using Bruker AVANCE III 400 WB spectrometer. Brunauer-Emmett-Teller (BET) surface area measurement were performed using Micromeritics ASAP2020 instrument at 77 K. Fourier Transform infrared (FT-IR) was conducted on a Bruker VERTEX70 spectrometer. Solid-state UV–vis diffuse reflectance spectra (UV–vis DRS) were recorded at room temperature on a Shimadzu UV-2700 spectrophotometer equipped with an integrating sphere attachment. Eelectron paramagnetic resonance (EPR) spectra were recorded on a Bruker EPR A300 spectrometer. Photoelectrochemical experiments were taken on a CHI660E workstation. X-ray photoelectron spectroscopy (XPS) measurements were performed on a Theta probe (Thermo Fisher) with Al Kα x-rays. Transmission electron microscopy (TEM) and energy-dispersive X-ray (EDX) spectroscopy were carried out on a Tecnai F20 at 200KV. High-angle annular dark-field (HAADF) images were acquired on a JEM-ARM200F. Scanning electron microscope (SEM) images were obtained on an Oxford X-max microscope. Steady-state photoluminescence (PL) and fluorescence decay spectra were measured on a FLS1000-Edinburgh Instruments. Thermogravimetric analysis (TGA) was carried out over a TGA Q500 thermal analysis system under air atmosphere. Inductively coupled plasma-atomic emission spectrometry (ICP-AES) (Shimadzu ICPS-7500) was used to determine the metal contents.

2.2. Photocatalytic measurements

The photocatalytic activity of samples for U(VI) reduction was evaluated in a photoreactor without any sacrificial agents under visible light irradiation from a 300 W xenon lamp (PerfectLight, PLS-SXE300D) with a 420 nm cut-off filter in the air atmosphere. Briefly, 10 mg of sample was firstly dispersed into the U(VI) solution (50 mL, 10 ppm). After reaction of certain time, aliquots of the dispersion were removed and filtered through a 0.45 μm membrane filter. The concentration of U(VI) in the filtrates was determined by UV–vis spectrophotometry using the Arsenazo III method at a wavelength of 650 nm. The organic and ion interference measurements were carried out in 10 ppm U(VI) solution with 1 ppm organics and 100 ppm interfering ions, respectively. In order to assess the reusability, the Cu_3-Ti_6-COF after reaction was collected and then poured into NaHCO$_3$ solution (50 mL, 0.1 mol/L) to ultrasound for 30 min. After that, the Cu_3-Ti_6-COF was washed using deionized water and dried at 100 °C under vacuum for next use. The removal ratio was calculated using the following equation of $(C_0 - C_t)/C_0 \times 100$ %, where C_t is the time concentrations of U(VI) (mg/L), C_0 is the initial concentrations of U(VI) (mg/L).
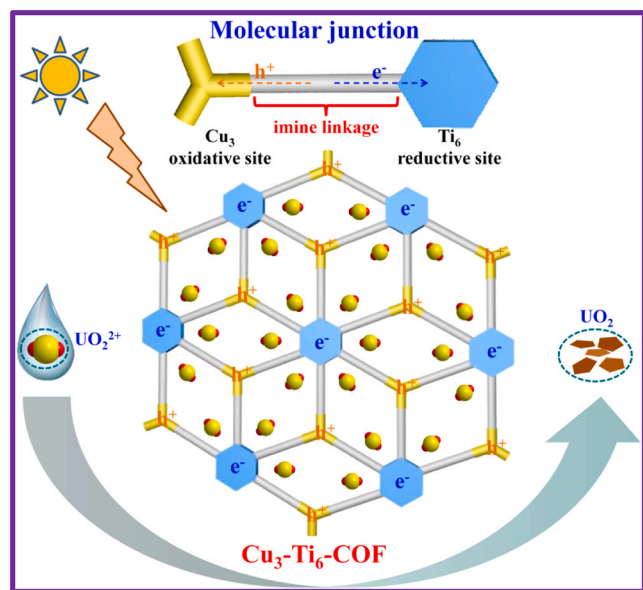
2.3. Calculation method

All calculations were performed by Gaussian 16 program package. The structure of Cu_3-Ti_6-COF and Cu_3-pA-COF were geometrically optimized by using the B3LYP method of density functional theory (DFT), where the basis sets for the Ti and Cu was LanL2dz [29] and for C, H, O, N was 6–31 G(d) [30]. Electrostatic potential (ESP) and front molecular orbitals were also calculated at the same level.

2.4. Synthesis of Ti_6 cluster

4-aminobenzoic acid (1.4 mmol 192.1 mg) and titanium (IV) isopropoxide (0.35 mmol, 103.6 μL) was firstly added into the autoclave with 6 mL 2-propanol and then stirred at room temperature for 30 min, followed by heating at 100 °C for 72 h. After reaction, the yellow octahedral crystals were collected, washed with 2-propanol and dried under vacuum at 70 °C for 3 h, which were denoted as Ti_6.

2.5. Synthesis of Cu_3 cluster

Cu(NO$_3$)$_2$·3 H$_2$O (0.83 mmol, 200 mg) and 1 H-PyCA (1.0 mmol,

Scheme 1. Schematic representation of Cu_3-Ti_6-COF molecular junction with high connectivity for photoreduction U(VI).

96 mg) were added into a mixed solvents of DMF (6.7 mL), deionized water (5 mL) and ethanol (6.7 mL) and then sonicated for 15 min to form a homogeneous dispersion, which was subsequently transferred into an autoclave (25 mL) with a Teflon liner and heated at 100 °C for 24 h. Afterwards, the light yellow crystals were obtained and immersed in deionized water for three days. In the meantime, the deionized water was exchanged 6 times per day. Finally, the crystals were washed quickly with acetone for several times and dried at 120 °C for 24 h under vacuum, which were denoted as Cu_3.

2.6. Synthesis of Cu₃-Ti₆-COF

Ti_6 (0.02 mmol, 31.1 mg) and Cu_3 (0.04 mmol, 19.8 mg) were added into a cylindrical glass tube (10 cm of length, ϕ_{in} = 2.2 cm, ϕ_{out} = 2.6 cm) with 1.8 mL mesitylene, 2 mL DMF and 0.2 mL 6 M acetic acid and then sonicated for 15 min. Afterwards, the mixture was flash frozen at 77 K in liquid nitrogen bath and degassed with three freeze-pump-thaw cycles for three times. After warming to room temperature, the mixture was heated at 120 °C for 72 h. The formed bright yellow precipitates (turn green in air) were immersed in DMF for 24 h to remove unreacted Cu_3. Then, the product was transferred to a Soxhlet extractor for washing with THF for 24 h, followed by drying at 100 °C under vacuum for 12 h.

2.7. Synthesis of Cu₃-pA-COF

p-Phenylenediamine (pA, 0.1 mmol, 11 mg) and Cu_3 cluster (0.07 mmol, 34 mg) were added into a cylindrical glass tube (10 cm of length, ϕ_{in} = 2.2 cm, ϕ_{out} = 2.6 cm) with *o*-dichlorobenzene (0.9 mL), DMF (0.1 mL) and acetic acid (6.4 µL), followed by ultrasonication for 15 min to get a homogeneous dispersion. After that, the mixture was flash frozen at 77 K in liquid nitrogen bath and degassed with three freeze-pump-thaw cycles. Upon naturally warming to room temperature, the mixture was heated at 120 °C for 72 h. The resulting crystalline powder was washed with DMF to remove the unreacted Cu_3 and pA and then transferred to a Soxhlet extractor for washing with THF for 24 h. Finally, the product was dried under vacuum at 120 °C for 12 h.

3. Results and discussion

The two building blcoks of Ti_6 and Cu_3 clusters were firstly designed and prepared to obtain Cu₃-Ti₆-COF molecular junction. The monomer of $Ti_6O_6(O^iPr)_6$(4-aminobenzoate)₆ (denoted Ti_6, OiPr = isopropoxide) was synthesized by solvothermal method using 4-aminobenzoic acid and titanium (IV) isopropoxide as raw materials [31]. The bright yellow octahedral crystalline product is obtained (Fig. S1). Another building block of $Cu_3(PyCA)_3 \cdot H_2O$ (denoted Cu_3, 1 H-PyCA = 1 H-pyrazolate-4-carboxaldehyde) was synthesized using Cu(NO3)$_2 \cdot 3 H_2O$ and 1 H-PyCA as reactant [32]. After reaction, the light yellow crystal of Cu_3 is observed, as revealed by the optical microscope image (Fig. S2). The FT-IR spectra of 4-aminobenzoic acid and Ti_6, as well as 1 H-PyCA and Cu_3 were presented in Fig. S3a. The Ti_6 and Cu_3 monomers present totally different spectra compared to 4-aminobenzoic acid and 1 H-PyCA, respectively. The stretching vibration peak related to C=O bond in 4-aminobenzoic acid was obviously detected at 1662 cm^{-1}, while it almost disappears in Ti_6, revealing the formation of coordination bonds between Ti node with the carboxyl group in 4-aminobenzoic acid [33]. In the case of 1 H-PyCA and Cu_3, the red shift of C=O stretching vibration in Cu_3 was detected compared to that in 1 H-PyCA, which should be attributed to the successful coordination of Cu to N site in 1 H-PyCA (Fig. S3b). Noticeably, PXRD patterns of Ti_6 and Cu_3 monomers match well with those reported (Fig. S4) [31,32], undoubtedly confirming the successful synthesis of two monomers.

Cu₃-Ti₆-COF was synthesized on the basis of Schiff-base condensation reaction between Ti_6 and Cu_3 building units through a solvothermal method at 120 °C for 72 h (Fig. 1). For comparison, the Cu₃-pA-COF
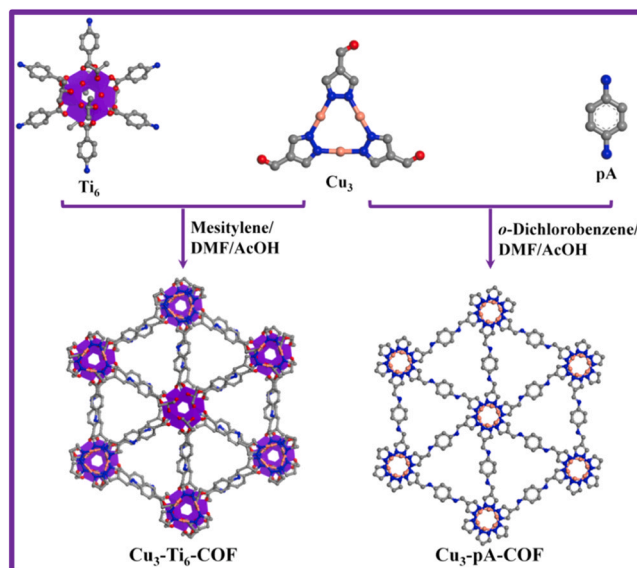

Fig. 1. The synthesis of Cu₃-Ti₆-COF and Cu₃-pA-COF.

sample was synthesized using pA instead of Ti_6 cluster to determine the merit of COFs molecular junction toward photocatalysis. PXRD measurements combined with the theoretical structural simulations were carried out to assess the crystallinity of Cu₃-Ti₆-COF and Cu₃-pA-COF. The R_3 space groups based on Cu₃-Ti₆-COF and Cu₃-pA-COF were constructed and Pawley refinement was applied by Materials Studio Software. The unit cell parameters of them are presented in Table S1. As shown in Fig. 2a, the strongest typical diffraction peak at 2 theta of 6.1° assigned to (110) crystalline plane of Cu₃-Ti₆-COF is observed. The (220), (330), (502), and (440) facets at 12.4°, 18.8°, 20.4°, and 25.3° also can be detected despite the weak intensity. Cu₃-pA-COF shows the typical peaks at 5.0°, 10.2°, 15.4°, 20.6° and 26.8° corresponding to the (110), (220), (330), (440) and (621) facets, respectively (Fig. 2b). Noticeably, the experimental XRD patterns of both Cu₃-Ti₆-COF and Cu₃-pA-COF match well with the simulated ABC stacking model (Fig. 2c, d), revealing the staggered stacking structure. The pore size in Cu₃-Ti₆-COF and Cu₃-pA-COF is estimated to be 0.597 and 0.598 nm with the interlayer distance of approximately 6.32 and 2.84 Å, respectively. Moreover, the negligible difference between the Rietveld refined PXRD patterns and the experimentally observed curves is illustrated by the negligible difference plot with low unweighted-profile R factor (R_p) (3.08 % for Cu₃-Ti₆-COF, 1.11 % for Cu₃-pA-COF) and weighted profile R factor (R_{wp}) (3.90 % for Cu₃-Ti₆-COF, 1.42 % for Cu₃-pA-COF).

The successful formation of imine linkage is confirmed by FT-IR and ^{13}C CP/MAS NMR spectra. As shown in Fig. 3a, Cu₃-Ti₆-COF exhibits much weaker signal assigned to C=O stretching vibration (1657 cm^{-1}) compared to Cu_3 [34], and N-H stretching vibration band (3200–3500 cm^{-1}) belonging to the amino group is absent in Cu₃-Ti₆--COF [35,36]. Importantly, the newly formed stretching vibration band at 1602 cm^{-1} assigned to C=N bond in Cu₃-Ti₆-COF appear [37]. In the case of Cu₃-pA-COF (Fig. S5), the N-H stretching signals (3297 and 3373 cm^{-1}) and the characteristic C=O stretching bonds (1657 cm^{-1}) assigned to pA and Cu_3 monomers disappear totally, respectively. As expected, the stretching band at 1610 cm^{-1} related to the C=N bond was detected in Cu₃-pA-COF. The FT-IR spectra strongly demonstrate the formation of imine linkage in Cu₃-Ti₆-COF and Cu₃-pA-COF *via* Schiff-base reaction. Furthermore, as verified by ^{13}C CP/MAS NMR spectra, the characteristic peak at about 150 ppm assigned to the carbon atom of C=N bond is distinctly observed in them (Fig. 3b, c), further indicative of the successful formation of covalent imine linkage [38]. The low-temperature N_2 adsorption-desorption measurements at 77 K were carried out to know the specific surface area and structural
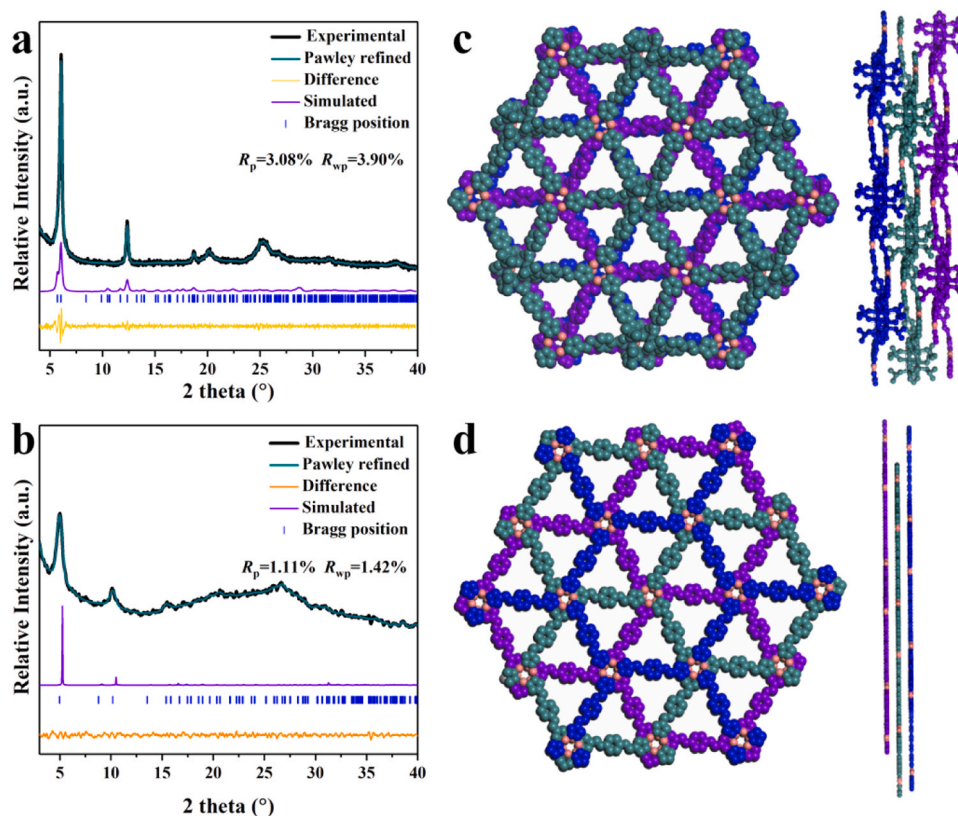
Fig. 2. PXRD patterns of Cu_3-Ti_6-COF (a) and Cu_3-pA-COF (b); Top (left) and side (right) views of the refined ABC structure of Cu_3-Ti_6-COF (c) and Cu_3-pA-COF (d).

porosity. The typical reversible adsorption-desorption isotherms are obtained in two COFs (Fig. 3d), reflecting the formation of micropores in them. The BET surface area of Cu_3-Ti_6-COF and Cu_3-pA-COF is measured to be about 221 and 135 $m^2 g^{-1}$, respectively, and the average pore size of 0.54 nm in Cu_3-Ti_6-COF and 0.58 nm in Cu_3-pA-COF obtained by nonlinear density functional theory (NLDFT) is well in accordance with the pore limiting diameter determined by the theoretical structural mode (Fig. S6). As observed by the SEM and TEM images, the Cu_3-Ti_6-COF exhibits the sheet-like morphology (Fig. 3e, f), which is totally different from the Cu_3 with needle-shaped structure and Ti_6 with regular octahedral morphology in Fig. S1, S2. The directional lattice fringes can be detected in Cu_3-Ti_6-COF by the high-resolution TEM (HRTEM) with the lattice spacing of 0.37 nm, which sufficiently demonstrates the high crystallinity of it [39]. Additionally, the energy-dispersive X-ray element mapping reveals the highly uniform distribution of Cu, Ti, C, N and O elements in Cu_3-Ti_6-COF (Fig. 3g).

The thermal stability of Cu_3-Ti_6-COF and Cu_3-pA-COF was measured by TGA, which can keep high thermal stability up to 270 °C (Fig. 4a). Furthermore, the chemical stability of Cu_3-Ti_6-COF is explored by PXRD patterns. As shown in Fig. 4b, the crystallinity and structure of Cu_3-Ti_6-COF is well remained after soaked in diverse solvents for 2 day. Furthermore, the chemical composition and valence state are disclosed by XPS measurements. As revealed by the XPS survey spectra (Fig. 4c), Cu_3-Ti_6-COF is composed of Cu, Ti, C, N and O elements, while the signal related to the Ti species was not detected in Cu_3-pA-COF. Furthermore, the high-resolution XPS spectra of Ti 2p in Cu_3-Ti_6-COF and Ti_6 are analyzed. The binding energy of Ti $2p_{3/2}$ in Ti_6 cluster is 458.7 eV, typical of Ti^{4+} species (Fig. 4d) [40,41]. For the Cu_3 monomer, the symmetrical Cu $2p_{3/2}$ signal at 932.9 eV is observed without the satellite peaks (Fig. 4e), indicative of the only Cu^+ species in Cu_3 monomer [42]. In the case of Cu_3-Ti_6-COF and Cu_3-pA-COF, the asymmetrical Cu $2p_{3/2}$ peaks with satellite peaks can be deconvoluted into two components of Cu^+ and Cu^{2+} species. The appearance of Cu^{2+} species is attributed to

the partial oxidation of Cu^+, which has no impact on the cyclic triangular skeleton of Cu_3 building unit in Cu_3-Ti_6-COF and Cu_3-pA-COF [43]. Noticeably, a positive shift of 0.4 eV for Cu $2p_{3/2}$ binding energy and a negative shift of Ti $2p_{3/2}$ binding energy by 0.4 eV is observed in Cu_3-Ti_6-COF compared to the corresponding Cu_3 and Ti_6 monomers, respectively. This result not only proves that the Cu_3 and Ti_6 building units are successfully covalently connected in Cu_3-Ti_6-COF, but also demonstrates the successful construction of an internal electric field [44]. In comparison, the Cu $2p_{3/2}$ binding energy of Cu^+ in Cu_3-pA-COF is almost identical to that in Cu_3 monomer, reflecting the weaker internal electric field in Cu_3-pA-COF with regard to that in Cu_3-Ti_6-COF. As a result, the self-assembling of Cu_3 and Ti_6 building units to construct Cu_3-Ti_6-COF molecular junction is more beneficial for the directed electron transport from Cu_3 to Ti_6 cluster, which may enhance the photocatalytic activity. Moreover, the XPS spectra of N 1 s are analyzed (Fig. 4f). Only one peak at the binding energy of 399.5 eV attributed to the pyrazole N was detected in Cu_3 monomer. In comparison, the high-resolution N 1 s spectra of Cu_3-Ti_6-COF and Cu_3-pA-COF are deconvoluted into two components. A new peak at 400.0 assigned to imine N is observed. The XPS spectra of C and O elements in Cu_3, Ti_6, Cu_3-pA-COF and Cu_3-Ti_6-COF are shown in Fig. S7, S8.

The photoelectro-chemical properties were studied to know the features of Cu_3-Ti_6-COF and Cu_3-pA-COF for potential photocatalytic applications. The transient photocurrent response was monitored to know the separating efficiency of carriers produced by visible light irradiation. As depicted in Fig. 5a, the obvious photocurrent signals were detected in all samples and the good reproducibility of the photocurrent intensity is confirmed during the on-off cycles. Notably, the photocurrent response of Cu_3-Ti_6-COF is 1.5 times higher than that in Cu_3-pA-COF, proving the higher photoinduced electron separation and transport efficiency in Cu_3-Ti_6-COF, which can donate more carries to the photocatalyst surface during the reaction process and thus enhance the photocatalytic activity [45]. The Ti_6 monomer exhibits obviously
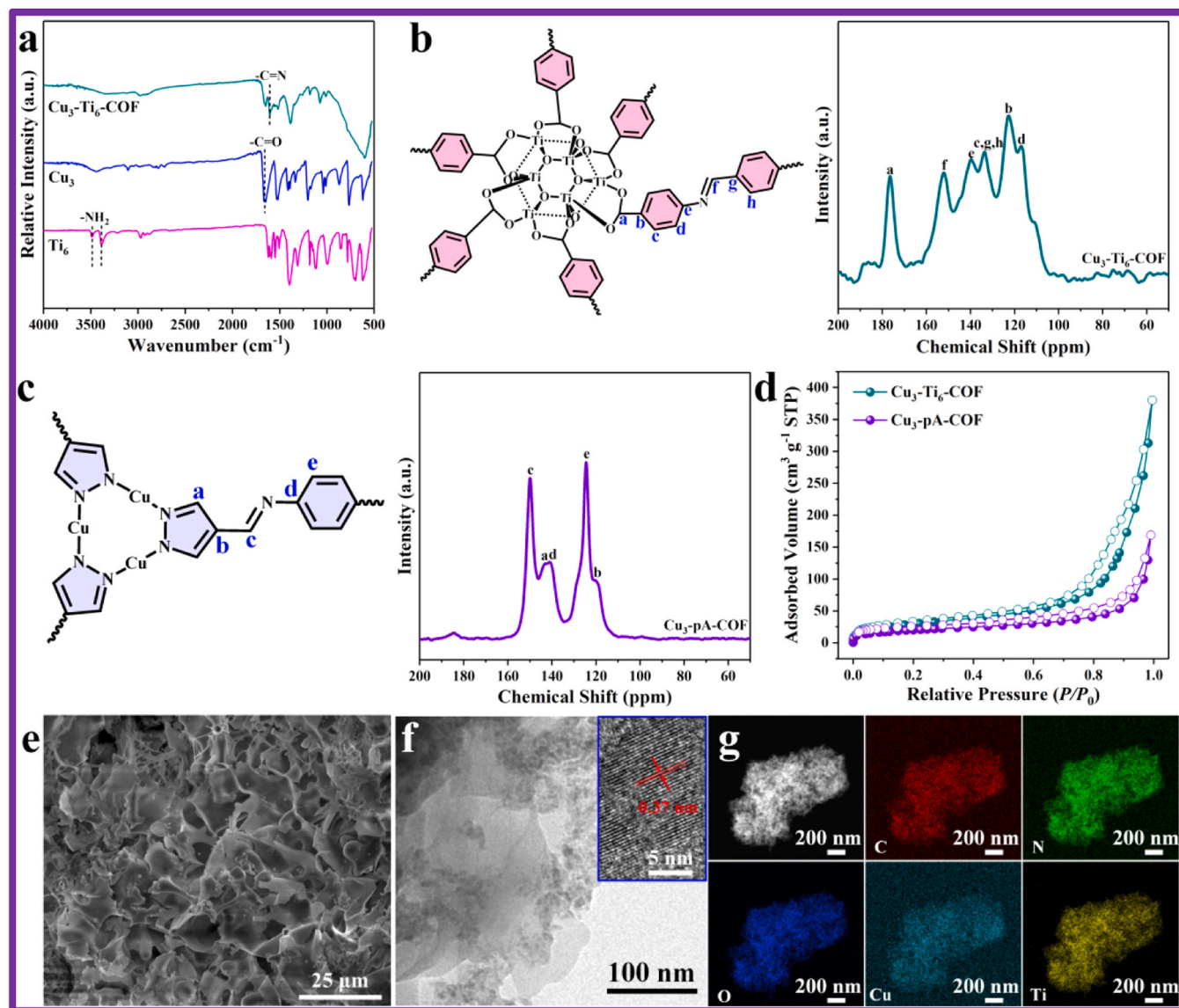
Fig. 3. FT-IR (a) and Solid-state ^{13}C NMR spectra (b, c); N_2 sorption isotherm at 77 K (d); SEM (e) and HRTEM images with lattice fringes (f); Element mapping of Cu_3-Ti_6-COF (g).

stronger photocurrent response than Cu_3 monomer, suggesting better photosensitivity of Ti_6 monomer. Electrochemical impedance spectroscopy (EIS) was also performed to investigate the charge transfer resistance. As disclosed by the Nyquist plots (Fig. 5b), the Cu_3-Ti_6-COF exhibits a smaller semicircle radius than Cu_3-pA-COF, implying the faster interfacial charge transfer rate in Cu_3-Ti_6-COF [46]. In addition, the charge separation behaviors of Cu_3-Ti_6-COF and Cu_3-pA-COF were further explored by the PL spectra (Fig. S9). The PL intensity in Cu_3-Ti_6-COF is significantly quenched compared to that in Cu_3-pA-COF, suggesting that the construction of molecular junction in Cu_3-Ti_6-COF can effectively hamper the recombination of photoinduced electron-hole pairs [47]. Furthermore, the fluorescence decay lifetimes of Cu_3-pA-COF and Cu_3-Ti_6-COF were measured to know the specific charge carrier dynamics (Fig. 5c and Table S2) [48]. The fast (τ_1) and slow (τ_2 and τ_3) excited-state lifetime are determined by the triple exponential function fitting. The surface trap states (τ_1) and the bulk energy/electron transfer (τ_2) results in the totally different lifetimes [49], while the slowest τ_3 may be ascribed to the energy/electron transfer along with the π-π stacking. The average decay lifetime of the photogenerated charge carriers in Cu_3-Ti_6-COF is estimated to be about

3.95 ns, which is longer than that in Cu_3-pA-COF (3.75 ns), proving the longer lifetime of generated charge carriers survived on the surface of Cu_3-Ti_6-COF to participate in the photocatalytic reaction [50]. Furthermore, the EPR measurements were taken to determine the generation of visible-light-induced charge carrier [51]. The stronger signal around g = 2.004 was detected in two COFs under visible light irradiation compared to those in the dark (Fig. 5d), which is attributed to the formation of conduction band electrons in them upon visible light excitation [52]. More importantly, the signal in Cu_3-Ti_6-COF is significantly stronger than that in Cu_3-pA-COF, indicating more outstanding ability to generate charge carriers in Cu_3-Ti_6-COF.

As revealed by UV–vis DRS in Fig. 5e, Cu_3-Ti_6-COF exhibits stronger absorption capability compared to other samples. Correspondingly, the optical band gaps (E_g) evaluated by Tauc plots are 2.29, 2.67, 2.96 and 2.41 eV in Cu_3-Ti_6-COF, Cu_3-pA-COF, Cu_3 and Ti_6, respectively (Fig. S10). Among four samples, Cu_3-Ti_6-COF shows the lowest bad gap, demonstrating that the least energy is needed to effectively separate the photogenerated charges [53]. Furthermore, the Mott-Schottky measurements were carried out to obtain the semiconductor character and flat band potentials [54]. All samples exhibits the positive slopes
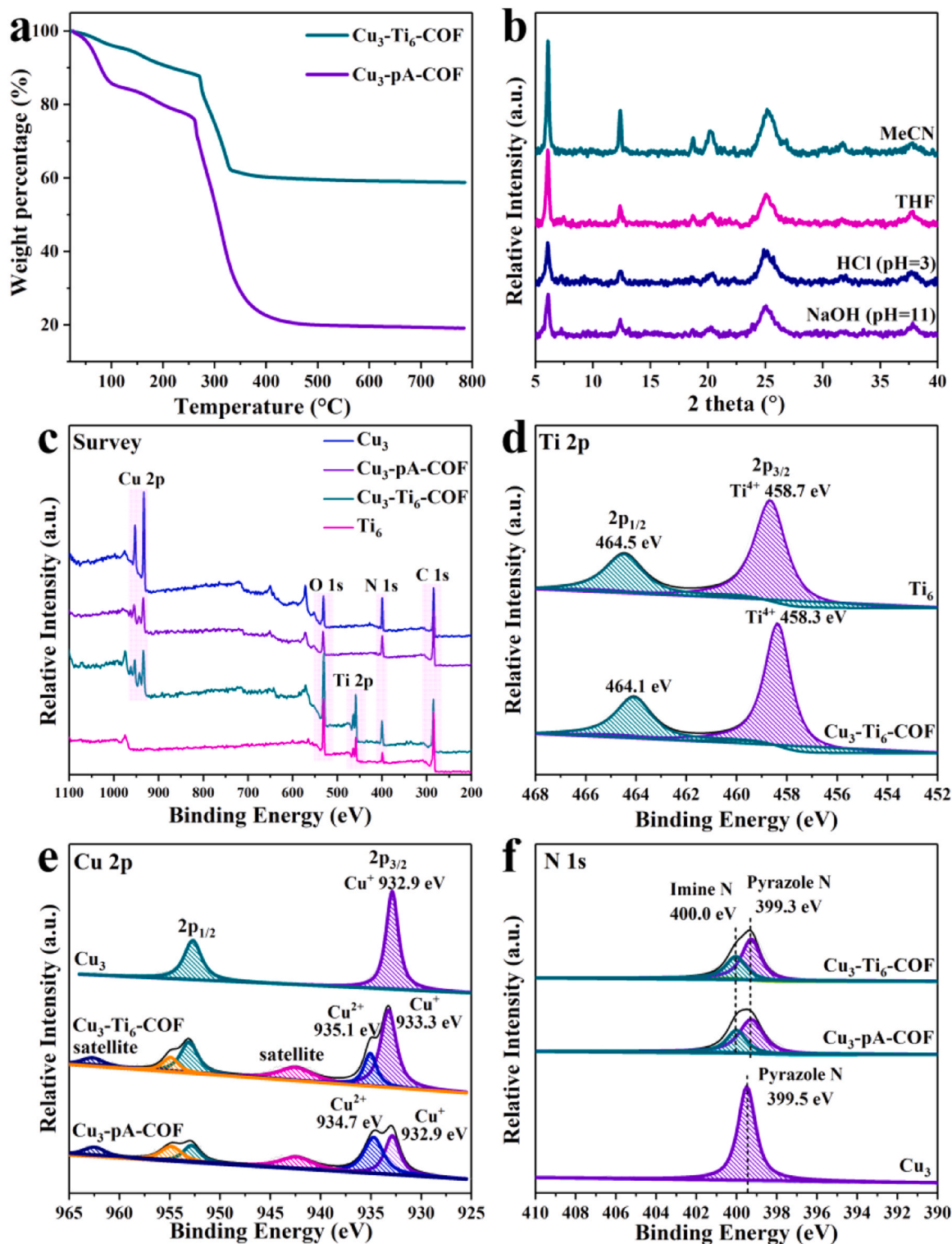
Fig. 4. TGA curves (a); PXRD pattern of Cu₃-Ti₆-COF after immersed in different solvents for 2 day (b); XPS spectra of survey (c), Ti 2p (d), Cu 2p (e) and N 1 s (f).

(Fig. S11), typical of *n*-type semiconductors. The flat band potentials are determined to be −0.94, −0.96, −1.14 and −0.34 V vs. Ag/AgCl (*i.e.* −0.74, −0.76, −0.94 and −0.14 V vs. NHE) in Cu₃-Ti₆-COF, Cu₃-pA-COF, Cu₃ and Ti₆, respectively, which are equal to their conduction band (CB) potentials. According to the equation of $E_g = E_{VB} - E_{CB}$, the valence band (VB) is calculated to be 1.55, 1.91, 2.02 and 2.27 V vs. NHE, respectively [55]. On the basis of these results, the energy band positions are plotted in Fig. 5f. More importantly, the CB position is more negative

than 0.41 V vs. NHE for U(VI)/U(IV) redox couple [56], meeting the thermodynamic requirement for photocatalytic reduction of U(VI) to U (IV). These photoelectro-chemical properties prove that designing spatially separated metal clusters as building unit to construct Cu₃-Ti₆-COF molecular junction can not only facilitate the capture of photogenerated electrons and holes, but also promote the separation and migration of charge carriers in the molecular junction framework, thus showing huge potential to improve photocatalytic efficiency of U
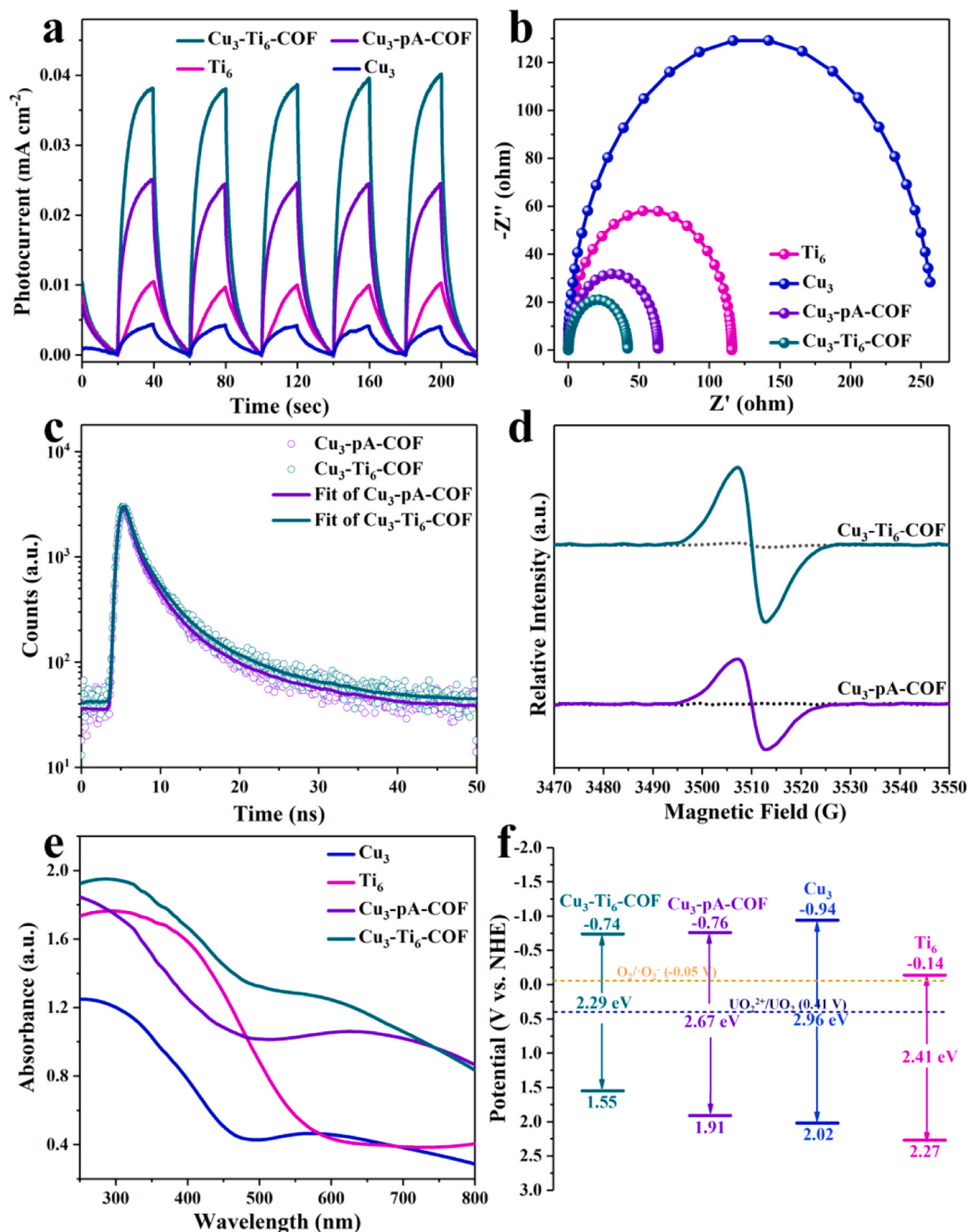
Fig. 5. Transient photocurrent response (a); Nyquist plots (b); Fluorescence decay lifetime (c); EPR conduction band electron spectra in the dark and under visible light irradiation (d); UV–vis DRS (e); Energy band position (f).

(VI) reduction.

The photocatalytic reduction experiments were carried out in U(VI)-simulated groundwater (10 ppm) under visible light irradiation and air atmosphere without any sacrificial agents. Unless otherwise specified, the sorbent concentration was fixed to be 0.2 g L^{-1}. Before the illumination of visible light, the reaction system was stirred in the dark for 90 min to reach the adsorption-desorption equilibrium. As shown in Fig. 6a, Cu$_3$-Ti$_6$-COF exhibits higher U(VI) removal ratio of 15.6 % in the dark than Cu$_3$-pA-COF (6.7 %), which is attributed to the stronger

adsorption ability of Cu$_3$-Ti$_6$-COF toward U(VI). Notably, upon the visible light irradiation, the U(VI) removal ratio increases sharply in both two COFs, and the Cu$_3$-Ti$_6$-COF delivers the significantly faster photocatalytic reaction kinetics than Cu$_3$-pA-COF. The reduction ratio in Cu$_3$-Ti$_6$-COF is as high as 94.8 % after visible-light irradiation for 210 min, which is much higher than that in Cu$_3$-pA-COF (45.9 %), indicating that the construction of molecular junction in Cu$_3$-Ti$_6$-COF based on two metal clusters actually improves the photocatalytic activity toward U(VI) reduction. Such high U(VI) removal ability achieved
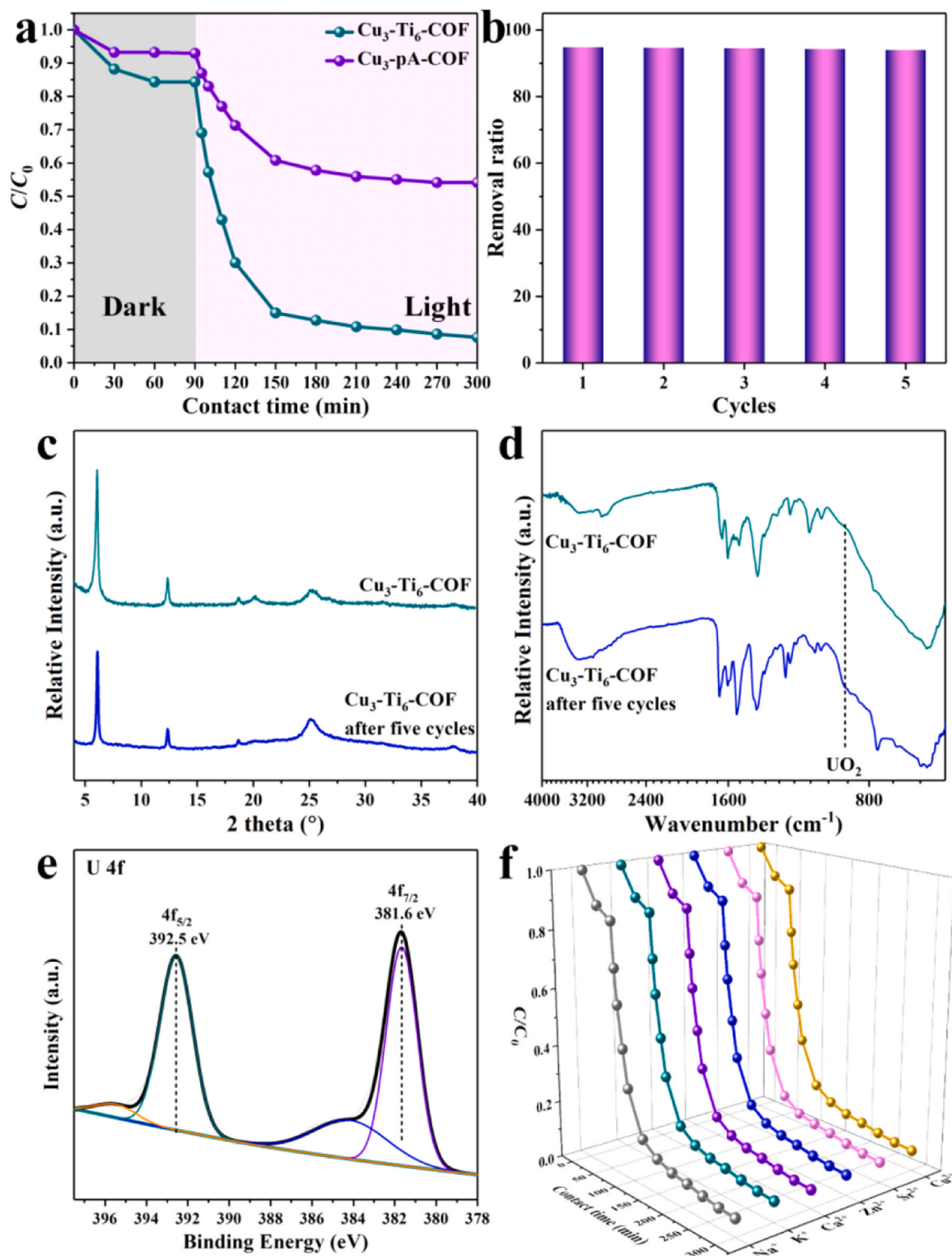
Fig. 6. The concentration of U(VI) over time in Cu$_3$-Ti$_6$-COF (a); U(VI) removal ratios during five successive reaction cycles (b); PXRD (c) and FT-IR (d) spectra of Cu$_3$-Ti$_6$-COF before and after five cycles; XPS spectrum of U 4 f in Cu$_3$-Ti$_6$-COF after reaction (e); The concentration of U(VI) over time with different coexisting ions (f).

under low solid-to-liquid ratio and without any sacrificial reagents makes Cu$_3$-Ti$_6$-COF outperforming most of the recently reported excellent photocatalysts (Table S3). The reusability of photocatalysts plays vital role for their practical application. As presented in Fig. 6b, after five cycles, Cu$_3$-Ti$_6$-COF still can keep an outstanding removal ratio of 94.1 %. A series of characterizations were performed for Cu$_3$-Ti$_6$-COF

after five cycles of use. PXRD (Fig. 6c) and FT-IR (Fig. 6d) prove the unchanged original structure. As revealed by the XPS measurement (Fig. S12), the binding energy of Cu$^+$ species in Cu$_3$-pA-COF after five uses is same to that in the initial one and higher than that in Cu$_3$ monomer, further confirming the structural stability during reaction process. The formation of uranium oxide species is confirmed in Cu$_3$-Ti$_6$-

COF after reaction by FT-IR and XPS spectra. The uranium element was detected in the XPS survey spectra (Fig. S13). In the high-resolution XPS spectrum of U 4 f (Fig. 6e), the peaks of U 4 $f_{7/2}$ and U 4 $f_{5/2}$ centered at 381.6 and 392.5 eV indicate the formation of U(IV) on the surface of Cu_3-Ti_6-COF after reaction [57]. ICP-AES result reveals that after five cycles only 0.28 % of Cu is leached from the Cu_3-Ti_6-COF.

Since the different U(VI) concentration in contaminated groundwater of each region, the photocatalytic activity of Cu_3-Ti_6-COF was evaluated ranging the U(VI) concentration from 1 to 300 ppm to know its applicable scope. As expected, Cu_3-Ti_6-COF exhibits remarkable photocatalytic performance in different U(VI) concentration (Fig. S14). Even in the U(VI) concentration of 300 ppm, the high removal ratio of 85.3 % is still achieved. In addition, the abundant F^- ions and organics are existed in the radioactive U(VI) wastewater generated from the nuclear power plants and nuclear fuel production, respectively [58,59]. Therefore, the effect of them on U(VI) removal performance was tested. Although the photocatalytic activity of Cu_3-Ti_6-COF gradually decreases with the increase of F^- content (Fig. S15), the removal ratio still can reach 90.3 % at high molar ratio of F: U (16: 1). A variety of organics such as bisphenol A (BPA), methylene blue (MB), tannic acid (TA) and rhodamine B (RhB) have negligible effect on photocatalytic activity of U(VI) reduction (Fig. S16). Furthermore, the effect of various cations including Na^+, K^+, Ca^{2+}, Zn^{2+}, Sr^{2+}, Cu^{2+} (100 ppm) were also explored. As shown in Fig. 6f, the high U(VI) removal ratio is well maintained in different coexisting ions. As a result, Cu_3-Ti_6-COF possesses outstanding photoreduction U(VI) ability under competing ions and organic interference.

As revealed by DFT simulations, the electron density of HOMO and LMUO is centered on the Cu_3 and Ti_6 clusters, respectively (Fig. 7a,b), which indicates the possible electron transfer from Cu_3 to Ti_6 unit upon visible-light excitation [60], well consistent with the XPS result. In comparison, when the Ti_6 unit is replaced by pA monomer, the electron density of LUMO mainly distributes on the Cu_3 unit (Fig. 7c,d). As revealed by ESP analysis, the negative potential regions are primarily distributed on the Ti-O cluster in Cu_3-Ti_6-COF (Fig. 7c) [61], while in the Cu_3-pA-COF, the negative potential regions are mainly concentrated on the Cu-N cluster (Fig. 7d). The DFT results demonstrate that constructing molecular junction in Cu_3-Ti_6-COF using metal-cluster building units is beneficial for the fabrication of strong internal electric field, which

promotes the electron transfer from Cu_3 to Ti_6, achieving the effective photoreduction of U(VI) in Ti-O cluster.

The active species during photocatalytic reduction of U(VI) in Cu_3-Ti_6-COF and Cu_3-pA-COF were investigated by scavenger measurements [62]. As shown in Fig. S17, the photocatalytic activity of Cu_3-Ti_6-COF is significantly inhibited after adding silver nitrate, *p*-benzoquinone and isopropanol to eliminate electron, superoxide radicals (•O_2^-) and hydroxyl radicals (•OH), respectively, reflecting that they are key active species toward U(VI) reduction. Moreover, EPR measurements were carried out to detect •O_2^-, singlet oxygen ($^1O_2$), and •OH during the photocatalytic reduction of U(VI). No any EPR signals were detected in Cu_3-Ti_6-COF and Cu_3-pA-COF under the dark condition. In comparison, the six consecutive characteristic peaks assigned to •O_2^- are observed in both Cu_3-Ti_6-COF and Cu_3-pA-COF (Fig. 8a). Noticeably, Cu_3-Ti_6-COF exhibits stronger •O_2^- signals than Cu_3-pA-COF, indicating more outstanding ability of Cu_3-Ti_6-COF to generate •O_2^- for U(VI) reduction. Moreover, the water oxidation half reaction also significantly influences the photocatalytic activity of U(VI) reduction half reaction because of its sluggish reaction kinetic related to multiple proton coupled electron transfer [63]. Thus, the water oxidation ability of Cu_3-Ti_6-COF and Cu_3-pA-COF is determined by the linear scanning voltammetry (LSV) curves measured at the electrolyte including U(VI) (8 ppm) and sodium chloride (0.5 M). As shown in Fig. 8b, Cu_3-Ti_6-COF exhibits more excellent activity compared to Cu_3-pA-COF, indicating more water oxidative active sites in Cu_3-Ti_6-COF. Furthermore, the •OH as crucial intermediate during water oxidation process was successfully detected in Cu_3-Ti_6-COF and Cu_3-pA-COF (Fig. 8c). As expected, the signal of it in Cu_3-Ti_6-COF is much stronger than that in Cu_3-pA-COF. The molecular junction of Cu_3-Ti_6-COF constructed by Ti_6 as reductive sites and Cu_3 as oxidative sites can produce more •OH and prevent the electron-hole recombination owing to the rapid consumption of photogenerated electron in Ti_6 surface toward U(VI) reduction. Moreover, the singlet oxygen ($^1O_2$) was also detected in Cu_3-Ti_6-COF and Cu_3-pA-COF (Fig. 8d) [64]. Similarly, the stronger signal is obtained in Cu_3-Ti_6-COF. The superior ability of Cu_3-Ti_6-COF to generate these reactive oxygen species through the interaction with O_2 under visible-light irradiation may effectively hamper the grown of microbes in the radioactive wastewater, thus ensuring the effective U(VI) reduction [57].

Based on the above results, we reasonly deduce that the excellent photocatalytic performance in Cu_3-Ti_6-COF is mainly ascribed to the following two factors. First, the molecular junction in Cu_3-Ti_6-COF enables the spatial periodical separation of the oxidative sites (Cu_3 cluster) and reductive sites (Ti_6 cluster) at the molecular level, which can effectively hinder the recombination of photogenerated electron-hole pairs, consequently resulting in the outstanding activity. Second, the strong internal electric field in Cu_3-Ti_6-COF promotes the directed electron transfer from Cu_3 to Ti_6 toward photoreduction U(VI).

4. Conclusion

In summary, a molecular junction COF (Cu_3-Ti_6-COF) with high connectivity, well-defined crystalline structure and monophasic periodic distribution was successfully synthesized through the covalent coupling of two metal clusters. The strong absorption in visible-light region, effective separation-efficiency of charge carriers and suitable photo-redox ability to drive U(VI) reduction is integrated in Cu_3-Ti_6-COF. Importantly, the molecular junction can promote the formation of internal electric field in Cu_3-Ti_6-COF framework, which is beneficial for the transfer of electrons from Cu_3 to Ti_6, achieving the simultaneous reactions of water oxidation on Cu_3 site and U(VI) reduction on electron-rich Ti_6 site. The U(VI) removal ratio in Cu_3-Ti_6-COF can reach as high as 94.8 % upon visible-light irradiation of 210 min without any sacrificial reagents, which is about 2.1 times higher than that in Cu_3-pA-COF synthesized using Cu_3 and pA as building units. Based on the experimental and theoretical results, we inferred that elaborately designing metal clusters as building blocks should be an effective strategy to
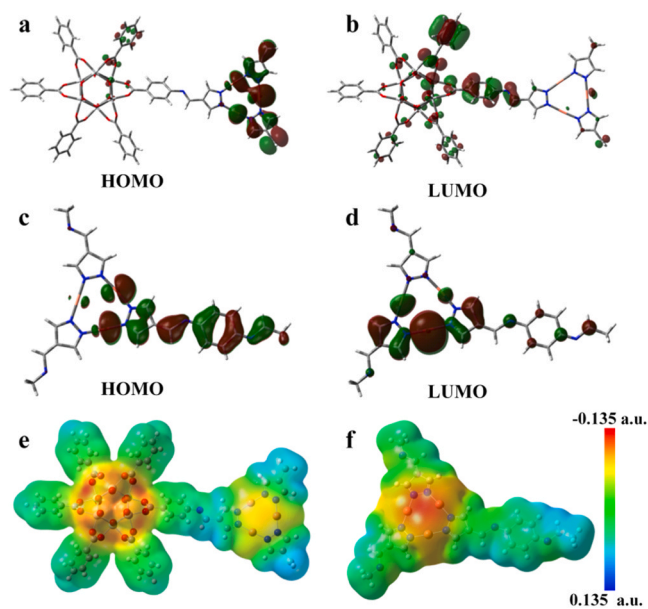

Fig. 7. The distribution of HOMO and LUMO orbits in Cu_3-Ti_6-COF (a, b) and Cu_3-pA-COF (c, d); Electrostatic potential of Cu_3-Ti_6-COF (e) and Cu_3-pA-COF (f).
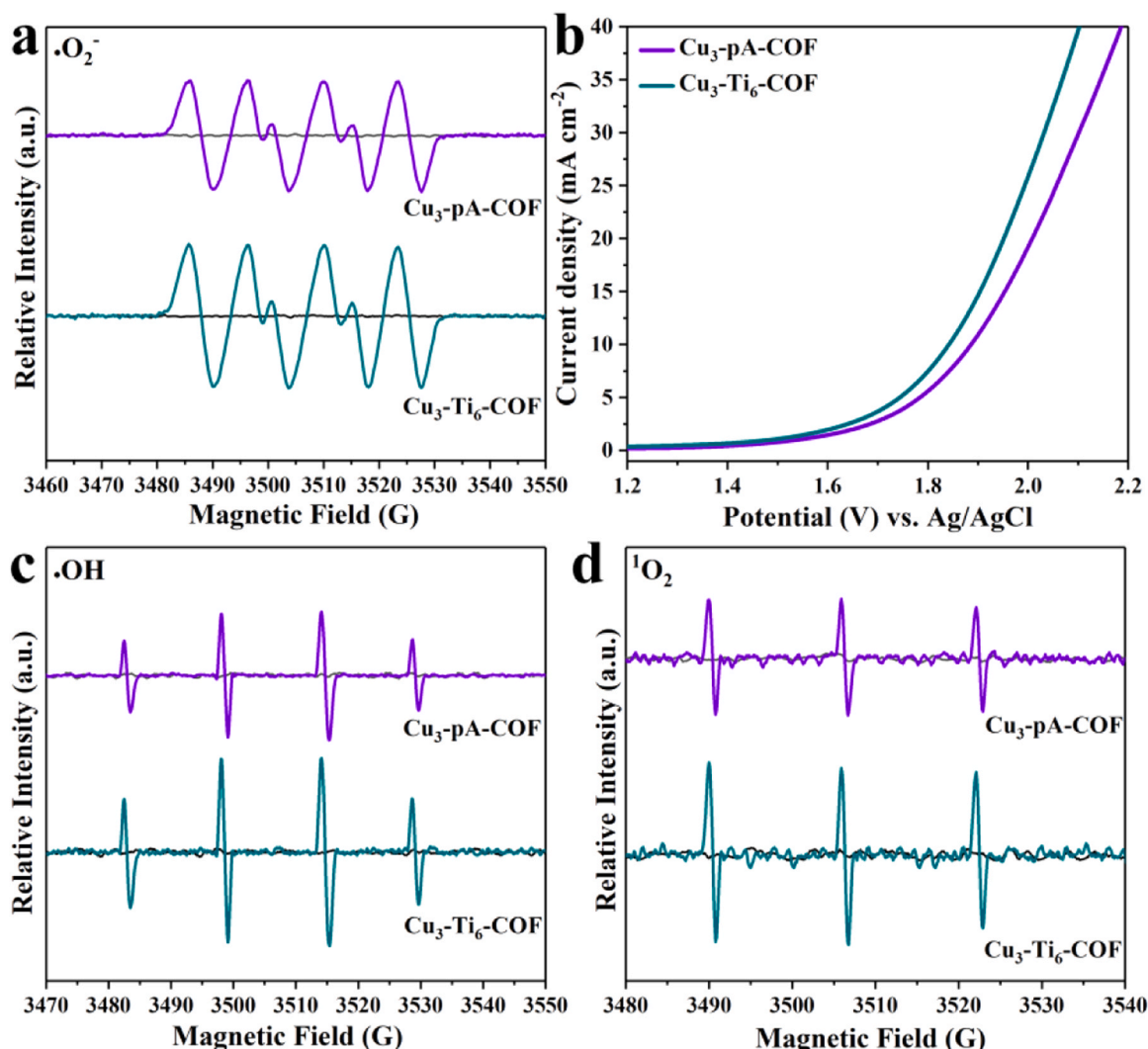
Fig. 8. EPR spectra of ●O₂ radical (a); LSV curves of water oxidation (b); EPR spectra of ●OH (c) and ¹O₂ (d).

fabricate and expand novel and highly efficient COFs molecular junction photocatalysts toward contaminant removal.

CRediT authorship contribution statement

Zhenzhen Xu: Methodology. **Jiajun Liao:** Data curation. **Zhuyao Li:** Data curation. **Yidong Luo:** Methodology. **Long-Shuai Zhang:** Writing – original draft. **Jian-Ping Zou:** Writing – review & editing. **zhi gao:** Writing – original draft, Conceptualization. **Yue Wang:** Data curation. **Zhaodi Sun:** Data curation.

Declaration of Competing Interest

There are no conflicts to declare.

Data Availability

Data will be made available on request.

Acknowledgments

Appendix A. Supporting information

Supplementary data associated with this article can be found in the online version at doi:10.1016/j.apcatb.2024.124053.

References

[1] X. Wang, X. Dai, C. Shi, J. Wan, M. Silver, L. Zhang, L. Chen, X. Yi, B. Chen, D. Zhang, K. Yang, J. Diwu, J. Wang, Y. Xu, R. Zhou, Z. Chai, S. Wang, Nat. Commun. 10 (2019) 2570.
[2] A. Satpathy, J.G. Catalano, D.E. Giammar, Environ. Sci. Technol. 56 (2022) 4111–4120.
[3] T. Liu, R. Zhang, M. Chen, Y. Liu, Z. Xie, S. Tang, Y. Yuan, N. Wang, Adv. Funct. Mater. 32 (2021) 2111049.
[4] D.S. Sholl, R.P. Lively, Nature 532 (2016) 435–437.
[5] C.W. Abney, R.T. Mayes, T. Saito, S. Dai, Chem. Rev. 117 (2017) 13935–14013.
[6] Y. Yuan, Y. Yang, X. Ma, Q. Meng, L. Wang, S. Zhao, G. Zhu, Adv. Mater. 30 (2018) 1706507.
[7] D. Beltrami, G. Cote, H. Mokhtari, B. Courtaud, B.A. Moyer, A. Chagnes, Chem. Rev. 114 (2014) 12002.
[8] Z. Li, Q. Meng, Y. Yang, X. Zou, Y. Yuan, G. Zhu, Chem. Sci. 11 (2020) 4747–4752.
[9] L. Yuan, M. Sun, X. Liao, Y. Zhao, Z. Chai, W. Shi, Sci. China Chem. 57 (2014) 1432–1438.
[10] X. Zhong, Q. Ling, Z. Ren, B. Hu, Appl. Catal. B: Environ. 326 (2023) 122398.

[11] Z.-J. Li, Z.-W. Huang, W.-L. Guo, L. Wang, L.-R. Zheng, Z.-F. Chai, W.-Q. Shi, Environ. Sci. Technol. 51 (2017) 5666–5674.
[12] H. Wang, H. Guo, N. Zhang, Z. Chen, B. Hu, X. Wang, Environ. Sci. Technol. 53 (2019) 6454–6461.
[13] M. Chen, T. Liu, X. Zhang, R. Zhang, S. Tang, Y. Yuan, Z. Xie, Y. Liu, H. Wang, K. V. Fedorovich, N. Wang, Adv. Funct. Mater. 31 (2021) 2100106.
[14] K. Yu, P. Jiang, H. Yuan, R. He, W. Zhu, L. Wang, Appl. Catal. B: Environ. 288 (2021) 119978.
[15] S. Liu, Z. Wang, Y. Lu, H. Li, X. Chen, G. Wei, T. Wu, D.-J. Maguire, G. Ye, J. Chen, Appl. Catal. B: Environ. 282 (2021) 119523.
[16] Y. Ye, J. Jin, F. Chen, D.D. Dionysiou, Y. Feng, B. Liang, H.-Y. Cheng, Z. Qin, X. Tang, H. Li, D. Yntema, C. Li, Y. Chen, Y. Wang, Chem. Eng. J. 450 (2022) 138317.
[17] M. Zhang, M. Lu, Z.-L. Lang, J. Liu, M. Liu, J.-N. Chang, L.-Y. Li, L.-J. Shang, M. Wang, S.-L. Li, Y.-Q. Lan, Angew. Chem. Int. Ed. 59 (2020) 6500–6506.
[18] P. Jiang, K. Yu, H. Yuan, R. He, M. Sun, F. Tao, L. Wang, W. Zhu, E J. Mater. Chem. A 9 (2021) 9809–9814.
[19] S. Karmakar, S. Barman, F.A. Rahimi, T.K. Maji, Energy Environ. Sci. 14 (2021) 2429–2440.
[20] K. Wu, X.-Y. Liu, P.-W. Cheng, Y.-L. Huang, J. Zheng, M. Xie, W. Lu, D. Li, J. Am. Chem. Soc. 145 (2023) 18931–18938.
[21] Y.H. Kim, J.-P. Jeon, Y. Kim, H.-J. Noh, J.-M. Seo, J. Kim, G. Lee, J.-B. Baek, Angew. Chem. Int. Ed. 62 (2023) e202307991.
[22] X. Zhong, Q. Ling, Z. Ren, B. Hu, Appl. Catal. B: Environ. 326 (2023) 122398.
[23] L. Chen, J. Hang, B. Chen, J. Kang, Z. Yan, Z. Wang, Y. Zhang, S. Chen, Y. Wang, Y. Jin, C. Xia, Chem. Eng. J. 454 (2023) 140378.
[24] X. Liu, R.-X. Bi, C.-R. Zhang, Q.-X. Luo, R.-P. Liang, J.-D. Qiu, Chem. Eng. J. 460 (2023) 141756.
[25] Y.-G. Wang, W. Jiang, X. Liu, L. Zhang, R.-P. Liang, J.-D. Qiu, Chem. Eng. J. 477 (2023) 146975.
[26] X. Zhong, Y. Liu, S. Wang, Y. Zhu, B. Hu, Sep. Purif. Technol. 279 (2021) 119627.
[27] L. Zhang, R.-H. Li, X.-X. Li, J. Liu, W. Guan, L.-Z. Dong, S.-L. Li, Y.-Q. Lan, Usa, P. Natl. Acad. Sci. 119 (2022) e2210550119.
[28] Q. Zhu, X. Wang, R. Clowes, P. Cui, L. Chen, M.A. Little, A.I. Cooper, J. Am. Chem. Soc. 142 (2020) 16842–16848.
[29] P.J. Hay, W.R. Wadt, J. Chem. Phys. 82 (1985) 270–283.
[30] R. Ditchfield, W.J. Hehre, J.A. Pople, J. Chem. Phys. 54 (1971) 724–728.
[31] K. Hong, H. Chun, Inorg. Chem. 52 (2013) 9705–9707.
[32] R.-J. Wei, H.-G. Zhou, Z.-Y. Zhang, G.-H. Ning, D. Li, CCS Chem. 3 (2020) 2045–2053.
[33] Z. Gao, Y. Lai, L. Gong, L. Zhang, S. Xi, J. Sun, L. Zhang, F. Luo, ACS Catal. 12 (2022) 9101–9113.
[34] X. Li, J. Wang, F. Xue, Y. Wu, H. Xu, T. Yi, Q. Li, Angew. Chem. Int. Ed. 60 (2021) 2534–2540.
[35] J.-N. Chang, Q. Li, Y. Yan, J.-W. Shi, J. Zhou, M. Lu, M. Zhang, H.-M. Ding, Y. Chen, S.-L. Li, Y.-Q. Lan, Angew. Chem. Int. Ed. 61 (2022) e202209289.
[36] J.-N. Chang, J.-W. Shi, Q. Li, S. Li, Y.-R. Wang, Y. Chen, F. Yu, S.-L. Li, Y.-Q. Lan, Angew. Chem. Int. Ed. 61 (2023) e202303606.
[37] H. Duan, X. Chen, Y.-N. Yang, J. Zhao, X.-C. Lin, W.-J. Tang, Q. Gao, G.-H. Ning, D. Li, J. Mater. Chem. A. 11 (2023) 12777–12783.
[38] T.-Y. Yu, Q. Niu, Y. Chen, M. Lu, M. Zhang, J.-W. Shi, J. Liu, Y. Yan, S.-L. Li, Y.-Q. Lan, J. Am. Chem. Soc. 145 (2023) 8860–8870.
[39] M. Zhang, P. Huang, J.-P. Liao, M.-Y. Yang, S.-B. Zhang, Y.-F. Liu, M. Lu, S.-L. Li, Y.-P. Cai, Y.-Q. Lan, Angew. Chem. Int. Ed. 62 (2023) e202311999.
[40] Z.-w Wang, Y.-z Shi, C. Liu, Y.-y Kang, L. Wu, Appl Catal, B: Environ. 301 (2022) 12080.
[41] M. Zhang, J.-N. Chang, Y. Chen, M. Lu, T.-Y. Yu, C. Jiang, S.-L. Li, Y.-P. Cai, Y.-Q. Lan, Adv. Mater. 33 (2021) 33 2105002.
[42] R.-J. Wei, P.-Y. You, H. Duan, M. Xie, R.-Q. Xia, X. Chen, X. Zhao, G.-H. Ning, A. I. Cooper, D. Li, J. Am. Chem. Soc. 144 (2022) 17487–17495.
[43] J. Cui, Y. Fu, J. Song, B. Meng, J. Zhou, Z. Zhou, Z. Su, ChemSusChem 16 (2023) e202202079.
[44] S. Zhang, L. Chen, Z. Qu, F. Zhai, X. Yin, D. Zhang, Y. Shen, H. Li, W. Liu, S. Mei, G. Ji, C. Zhang, X. Dai, Z. Chai, S. Wang, Chem 9 (2023) 3172–3184.
[45] G. Zhou, Y. Xu, Y. Cheng, Z. Yu, B. Wei, X. Liu, Z. Chen, C. Li, Z. Lu, Appl. Catal. B: Environ. 335 (2023) 122892.
[46] C. Qin, X. Wu, L. Tang, X. Chen, M. Li, Y. Mou, B. Su, S. Wang, C. Feng, J. Liu, X. Yuan, Y. Zhao, H. Wang, Nat. Commun. 14 (2023) 5238.
[47] R. Dai, X. Chen, N. Ouyang, Y. Hu, Chem. Eng. J. 431 (2022) 134172.
[48] L.-L. Zheng, L. Tian, L.-S. Zhang, J. Yu, Y. Chen, Q. Fu, X.-Z. Liu, D.-S. Wu, J.-P. Zou, ACS Catal. 14 (2024) 2134–2143.
[49] X. Jiao, Z. Chen, X. Li, Y. Sun, S. Gao, W. Yan, C. Wang, Q. Zhang, Y. Lin, Y. Luo, Y. Xie, J. Am. Chem. Soc. 139 (2017) 7586.
[50] K. Yu, L. Tang, X. Cao, Z. Guo, Y. Zhang, N. Li, C. Dong, X. Gong, T. Chen, R. He, W. Zhu, Adv. Funct. Mater. 32 (2022) 2200315.
[51] Y. Xu, Y. Ren, G. Zhou, S. Feng, Z. Yang, S. Dai, Z. Lu, T. Zhou, Adv. Funct. Mater. (2024) 2313695, https://doi.org/10.1002/adfm.202313695.
[52] Z. Chen, J. Wang, M. Hao, Y. Xie, X. Liu, H. Yang, G.I.N. Waterhouse, X. Wang, S. Ma, Nat. Commun. 14 (2023) 1106.
[53] W.-R. Cui, C.-R. Zhang, R.-H. Xu, X.-R. Chen, R.-H. Yan, W. Jiang, R.-P. Liang, J.-D. Qiu, Small 17 (2021) 2006882.
[54] J.-P. Zou, D.-D. Wu, J. Luo, Q.-J. Xing, X.-B. Luo, W.-H. Dong, S.-L. Luo, H.-M. Du, S.L. Suib, ACS Catal. 6 (2016) 6861–6867.
[55] Z. Gao, Y. Wang, Y. Lin, Z. Zheng, Y. Liu, Q. Jing, F. Luo, Sci. China Chem. 65 (2022) 1544–1551.
[56] M. Hao, Z. Chen, X. Liu, X. Liu, J. Zhang, H. Yang, G.I.N. Waterhouse, X. Wang, S. Ma, CCS Chem. 4 (2022) 2294–2307.
[57] H. Yang, M. Hao, Y. Xie, X. Liu, Y. Liu, Z. Chen, X. Wang, G.I.N. Waterhouse, S. Ma, Angew. Chem. Int. Ed. 62 (2023) e202303129.
[58] J. Zhou, J. Yu, H. Liao, Y. Zhang, X. Luo, Sep. Sci. Technol. 55 (2020) 658–671.
[59] L. Wu, L. Zhang, R. Liu, H. Ge, Z. Tao, Q. Meng, Y. Zhang, T. Duan, ACS EST Water 1 (2021) 2197–2205.
[60] W. Huang, Y. Hu, Z. Qin, Y. Ji, X. Zhao, Y. Wu, Q. He, Y. Li, C. Zhang, J. Lu, Y. Li, Natl. Sci. Rev. 10 (2023) 171.
[61] Y. Cheng, J. Jin, H. Yan, G. Zhou, Y. Xu, L. Tang, X. Liu, H. Li, K. Zhang, Z. Lu, Angew. Chem. Int. Ed. (2024) e202400857, https://doi.org/10.1002/anie.202400857.
[62] X. Cao, K. Yu, Y. Zhang, N. Li, P. Wang, L. Zhou, X. Gong, H. Wang, F. Yang, W. Zhu, R. He, ACS Appl. Mater. Interfaces 15 (2023) 1063–1072.
[63] F.Q. Liu, J.W. Liu, Z. Gao, L. Wang, X.-Z. Fu, L.X. Yang, Y. Tao, W.H. Yin, F. Luo, Appl. Catal. B: Environ. 258 (2019) 117973.
[64] L.-S. Zhang, X.-H. Jiang, Z.-A. Zhong, L. Tian, Q. Sun, Y.-T. Cui, X. Lu, J.-P. Zou, S.-L. Luo, Angew. Chem. Int. Ed. 60 (2021) 21751–21755.